Avoiding Lockout Instability for Towed Parafoil Systems

Carlos Montalvo*
University of South Alabama, Mobile, Alabama 36688
and
Mark Costello†
Georgia Institute of Technology, Atlanta, Georgia 30332

DOI: 10.2514/1.G001545

Many towed systems consist of a parent platform moving along the ground, air, or water surface connected to a towed vehicle via a tether line. Motion of a towed parafoil system can be complex and is driven by motion of the parent platform, canopy control inputs, and wind disturbances. A particularly problematic flight dynamic instability for this system is canopy lockout, in which the canopy attains a large lateral offset and bank angle resulting in high line tension. It is possible to use left and right brakes to return the system to its nominal position; however, if the lateral offset and bank angle are too large, it is not possible to restore the system to a nominal position, and the lateral offset and bank angle grows until impact with a ground surface. This paper explores the lockout phenomena using a multibody simulation and identifies passive means to avoid the instability by locating the tether connection point forward on the cradle in combination with sufficiently high cradle–canopy yaw stiffness. Moreover, it is shown that an active control system that regulates canopy roll angle with parafoil brake inputs can eliminate the instability for the tested configuration.

Nomenclature

A, B, C	=	Lamb's coefficients for apparent mass, kg
b	=	canopy span, m
$C_B(\boldsymbol{v})$	=	component operator for a vector $\boldsymbol{\nu}$ in frame B
d	=	canopy arc radius, m
F^B	=	force applied to system in B frame, N
M^B	=	moment applied to system in B frame, N · m
$[I]$	=	identity matrix
$[I_T]$	=	total system inertia matrix, kg · m^2
L, M, N	=	components of moment vector in the body reference frame, N · m
m	=	mass of subsystem, kg
P, Q, R	=	Lamb's coefficients for apparent inertia, kg · m^2
p, q, r	=	angular velocity components in the body reference frame, rad/s
$\tilde{p}, \tilde{q}, \tilde{r}$	=	angular velocity components in the canopy reference frame, rad/s
S	=	aerodynamic reference area, m^2
$S_B(\boldsymbol{v})$	=	skew symmetric cross product operator for a vector $\boldsymbol{\nu}$ expressed in frame B
T_{IB}	=	transformation matrix from inertial frame to body frame
$T_{B,i}$	=	transformation matrix from body frame to ith canopy panel frame
u, v, w	=	velocity components of mass center in the body reference frame, m/s
$\tilde{u}, \tilde{v}, \tilde{w}$	=	velocity components with respect to the air, m/s
x, y, z	=	inertial positions of the system mass center, m
X, Y, Z	=	components of force in the body reference frame, N
α_i	=	angle of attack of the ith panel, rad
β	=	sideslip angle, rad
δ	=	dimensionless control deflection
φ, θ, ψ	=	Euler roll, pitch, and yaw angles, rad
χ	=	azimuth angle (course over ground), rad

Subscripts

A	=	aerodynamic
AM	=	apparent mass
C	=	cradle body frame
i	=	ith panel of the canopy
P	=	parafoil body frame
W	=	weight

I. Introduction

TOWED systems that consist of a moving platform and a towed body are used in a diverse set of scenarios, including wind energy extraction, entertainment, reconnaissance, communication, and surveillance [1]. A towed parafoil and payload system is composed of a parafoil and cradle combination connected via a tether. The tether is connected to a parent platform such as a ground vehicle, water vessel, or a fixed point. The ram-air parafoil uses incoming air to inflate the parachute into a winglike structure, giving the system a relatively large lift-to-drag ratio [2].

A particularly problematic flight dynamic instability is canopy lockout, in which the canopy attains a large lateral offset and bank angle, resulting in high line tension [3]. If an atmospheric disturbance or the pilot/active control system steers the parafoil away from the tether line of action, or if the bank angle grows, the canopy bank angle and lateral offset will continue to grow until the canopy impacts the ground or the tether line fails (Fig. 1). If the bank angle and lateral offset are too large, it is not possible to return the system to its nominal position, and the instability can only be mitigated by releasing the tow line from the towed parafoil so that the parafoil returns to an open loop glide. In some situations, lockout instability can be mitigated by reducing line tension through timely tether line payout [4].

The lockout problem has been considered in the literature by several authors. The work done by Terink, Breukel, Schmehl, and Ockels [5] examined the flight dynamics and stability of a tethered inflatable kiteplane. They showed a direct relationship between the wing dihedral angle and vertical tail plane size to the stability of towed flight using a 5 degree-of-freedom (DOF) model. Puranik [4] performed a linear model analysis of different trim conditions of a parafoil payload system as a function of atmospheric disturbances. This work involved a complete static analysis based on different

Received 25 June 2015; revision received 16 October 2015; accepted for publication 17 October 2015; published online 7 January 2016.

*Assistant Professor, College of Engineering, Mechanical Engineering. Member AIAA.

†David S. Lewis Professor of Autonomy, Guggenheim School of Aerospace Engineering, Woodruff School of Mechanical Engineering.

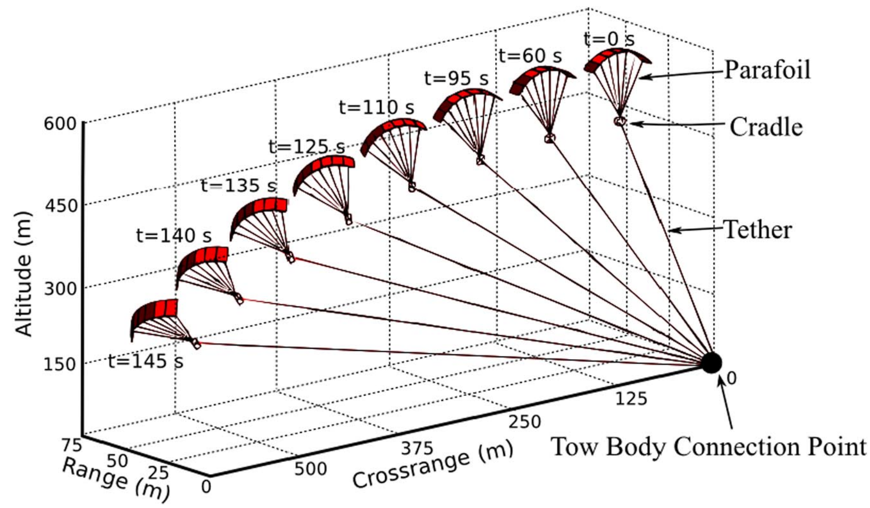

Fig. 1 Towed system schematic with example lockout condition (parafoil and cradle not to scale).

control inputs. A full state feedback controller was used to increase the stability envelope of the system.

Research characterizing parafoil lockout have all employed 5 DOF models using two tether angles and three Euler angles for the parafoil and cradle system. These models do not include relative rotation between the cradle and the canopy, which can substantially affect lockout mode stability. This paper explores the parafoil lockout phenomena with a focus on both passive changes to the parafoil and cradle system to increase the stable operating region of the system and active roll control to expand the flight envelope of a towed system. The paper begins by defining the system dynamic model, composed of a 9 DOF parafoil and cradle model coupled to a tether bead model. The simulation is subsequently employed to explore practical and implementable passive geometric changes to the system and active control to eliminate the lockout instability. Note, in this analysis the tether parameters are held constant.

II. System Dynamic Model

The multibody system has three major parts: the parafoil, cradle, and tether (Fig. 1). The isolated parafoil and cradle are represented with 9 DOFs. The parafoil and cradle are each modeled as rigid bodies connected via a gimbal joint located at the confluence point. The tether is modeled as a multibody system by discretizing the tether into N beads, with each bead connected to each other with a standard linear solid elastic element. Finally, a tow vehicle is assumed to be traveling with known motion.

A. Parafoil and Cradle Dynamic Model

Figure 2 shows a schematic of the isolated parafoil and cradle [6]. In this model, a gimbal joint couples the parafoil and cradle components at point G. This gimbal joint allows both the parafoil and the cradle to rotate freely about joint G, while still being constrained by the force and moment at the joint. The parafoil is connected to the gimbal joint via a rigid massless rod from the center of mass of the parafoil to point G. Similarly, the cradle is connected to the gimbal joint via another rigid massless rod. In practice, this system would contain multiple rigging lines called risers, emanating from the parafoil and connecting to the cradle at riser connection joints. The distance from the parafoil and cradle center of mass to the gimbal joint is denoted as WL Parafoil and WL Cradle, respectively. With the

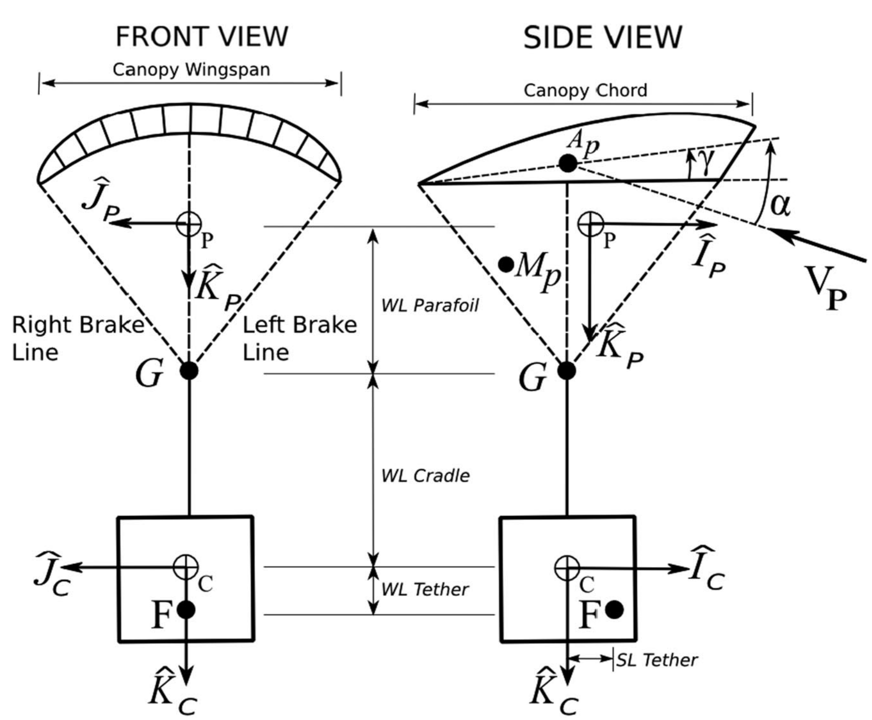

Fig. 2 Schematic of parafoil and cradle dynamic model (not to scale).

exception of movable parafoil brakes, the parafoil canopy is considered to be a rigid body once it has completely inflated. The model, however, breaks the canopy into multiple flat-plate panels and computes lift and drag at each panel. The total aerodynamic force is then the summation of all forces on each panel. Figure 2 shows the left and right brake lines, which modify the aerodynamic characteristics of the canopy to increase lift and drag on the canopy. The origin of the cradle frame is located at the center of mass of the cradle, with the $\hat{\boldsymbol{I}}_C$ unit vector pointing forward and the $\hat{\boldsymbol{J}}_C$ unit vector pointing toward the right side. The $\hat{\boldsymbol{K}}_C$ unit vector is oriented downward to complete the orthonormal basis. The origin of the parafoil frame is also located at the center of mass of the parafoil. The $\hat{\boldsymbol{I}}_P$ unit vector is oriented forward. The angle between the $\hat{\boldsymbol{I}}_P$ unit vector and the mean camber line of the canopy is denoted as the incidence angle of the canopy. The $\hat{\boldsymbol{J}}_P$ unit vector is oriented to the right side of the parafoil and the $\hat{\boldsymbol{K}}_P$ unit vector is oriented downwards to complete the orthonormal basis.

The tether line is connected to the cradle at point F. The forward and downward distance from the center of mass of the cradle to the tether connection point are denoted as WL Tether and SL Tether, respectively. The coordinates used to model the parafoil and cradle are three inertial position components of the joint $G(x_G, y_G, z_G)$, as well as the three Euler orientation angles of the parafoil canopy (ϕ_P, θ_P, ψ_P) and the cradle (ϕ_C, θ_C, ψ_C). The development of this model follows Slegers and Costello [6]. The kinematic equations for the parafoil canopy and the cradle are provided in Eqs. (1–3)

$$\begin{Bmatrix} \dot{x}_G \\ \dot{y}_G \\ \dot{z}_G \end{Bmatrix} = T_{IP}^T(\phi_P, \theta_P, \psi_P) \begin{Bmatrix} u_G \\ \boldsymbol{v}_G \\ w_G \end{Bmatrix} \tag{1}$$

$$\begin{Bmatrix} \dot{\phi}_c \\ \dot{\theta}_c \\ \dot{\psi}_c \end{Bmatrix} = H(\phi_c, \theta_c, \psi_c) \begin{Bmatrix} p_c \\ q_c \\ r_c \end{Bmatrix} \tag{2}$$

$$\begin{Bmatrix} \dot{\phi}_P \\ \dot{\theta}_P \\ \dot{\psi}_P \end{Bmatrix} = H(\phi_P, \theta_P, \psi_P) \begin{Bmatrix} p_P \\ q_P \\ r_P \end{Bmatrix} \tag{3}$$

in which the matrices T and H relate the body linear and angular velocity components to the position of the gimbal joint and Euler angles of the parafoil and cradle as given by Eq. (4) [7]

$$T_{IP}^T(\phi, \theta, \psi) = \begin{bmatrix} c_\theta c_\psi & s_\phi s_\theta c_\psi - c_\phi s_\psi & c_\phi s_\theta c_\psi + s_\phi s_\psi \\ c_\theta s_\psi & s_\phi s_\theta s_\psi + c_\phi c_\psi & c_\phi s_\theta s_\psi - s_\phi c_\psi \\ -s_\theta & s_\phi c_\theta & c_\phi c_\theta \end{bmatrix}$$
$$H(\phi, \theta, \psi) = \begin{bmatrix} 1 & s_\phi t_\theta & c_\phi t_\theta \\ 0 & c_\phi & -s_\phi \\ 0 & s_\phi / c_\theta & c_\phi / c_\theta \end{bmatrix} \tag{4}$$

The dynamic equations are formed by first separating the system at the coupling joint, exposing the joint constraint force acting on both bodies. The translational and rotational dynamic equations are written for each body individually, creating a set of four vector equations. Note that the cradle contains forces and moments from the tether

$$m_P \boldsymbol{a}_{\oplus_P/I} = \boldsymbol{F}_A^P - \boldsymbol{F}_{\mathrm{AM}}^P + \boldsymbol{F}_W^P - \boldsymbol{F}_G \tag{5}$$

$$m_C \boldsymbol{a}_{\oplus_C/I} = \boldsymbol{F}_A^C + \boldsymbol{F}_W^C + \boldsymbol{F}_G + \boldsymbol{F}_{T_{n_T}} \tag{6}$$

$$\frac{{}^I \mathrm{d}\boldsymbol{H}_{\oplus_{P/I}}}{\mathrm{d}t} = \boldsymbol{M}_A^P - \boldsymbol{M}_{\mathrm{AM}}^P - \boldsymbol{M}_G + \sum_{i=1}^{N} \boldsymbol{r}_{\oplus_P \to A_i} \times \boldsymbol{F}_{A_i}^P - \boldsymbol{r}_{\oplus_P \to M_p} \times \boldsymbol{F}_{\mathrm{AM}}^P - \boldsymbol{r}_{\oplus_P \to G} \times \boldsymbol{F}_G \tag{7}$$

$$\frac{{}^I \mathrm{d}\boldsymbol{H}_{\oplus_{C/I}}}{\mathrm{d}t} = \boldsymbol{M}_G + \boldsymbol{r}_{\oplus_C \to G} \times \boldsymbol{F}_G + \boldsymbol{r}_{\oplus_C \to F} \times \boldsymbol{F}_{T_{n_T}} \tag{8}$$

The vectors $\boldsymbol{r}_{\oplus_P \to A_i}$, $\boldsymbol{r}_{\oplus_P \to M_p}$, and $\boldsymbol{r}_{\oplus_P \to G}$ are vectors from the center of mass of the parafoil to the aerodynamic center of the ith panel, apparent mass center, and gimbal joint G, respectively. The vectors $\boldsymbol{r}_{\oplus_C \to G}$ and $\boldsymbol{r}_{\oplus_C \to F}$ are vectors from the center of mass of the cradle to the gimbal joint G and to the connection point of the tether, respectively. The acceleration and angular momentum time derivative expressions in the translational and rotational dynamic equations are described below:

$$\boldsymbol{a}_{\oplus_P/I} = a_{xp} \hat{I}_P + a_{yp} \hat{J}_P + a_{zp} \hat{K}_P \tag{9}$$

$$\boldsymbol{a}_{\oplus_C/I} = a_{xc} \hat{I}_C + a_{yc} \hat{J}_C + a_{zc} \hat{K}_C \tag{10}$$

$$\frac{{}^I \mathrm{d}\boldsymbol{H}_{\oplus_{P/I}}}{\mathrm{d}t} = h_{xp} \hat{I}_P + h_{yp} \hat{J}_P + h_{zp} \hat{K}_P \tag{11}$$

$$\frac{{}^I \mathrm{d}\boldsymbol{H}_{\oplus_{C/I}}}{\mathrm{d}t} = h_{xp} \hat{I}_C + h_{yp} \hat{J}_C + h_{zp} \hat{K}_C \tag{12}$$

in which

$$\begin{Bmatrix} a_{xp} \\ a_{yp} \\ a_{zp} \end{Bmatrix} = \begin{Bmatrix} \dot{u}_G \\ \dot{v}_G \\ \dot{w}_G \end{Bmatrix} + S_P(\boldsymbol{\omega}_{P/I}) \begin{Bmatrix} u_G \\ v_G \\ w_G \end{Bmatrix} + S_P(\boldsymbol{r}_{\oplus_P \to G}) \begin{Bmatrix} \dot{p}_P \\ \dot{q}_P \\ \dot{r}_P \end{Bmatrix} - S_P(\boldsymbol{\omega}_{P/I}) S_P(\boldsymbol{\omega}_{P/I}) \begin{Bmatrix} x_{PG} \\ y_{PG} \\ z_{PG} \end{Bmatrix} \tag{13}$$

$$\begin{Bmatrix} a_{xc} \\ a_{yc} \\ a_{zc} \end{Bmatrix} = T_{IC} T_{IP}^T \left(\begin{Bmatrix} \dot{u}_G \\ \dot{v}_G \\ \dot{w}_G \end{Bmatrix} + S_P(\boldsymbol{\omega}_{P/I}) \begin{Bmatrix} u_G \\ v_G \\ w_G \end{Bmatrix} \right) + S_C(\boldsymbol{r}_{\oplus_C \to G}) \begin{Bmatrix} \dot{p}_C \\ \dot{q}_C \\ \dot{r}_C \end{Bmatrix} - S_C(\boldsymbol{\omega}_{C/I}) S_C(\boldsymbol{\omega}_{C/I}) \begin{Bmatrix} x_{CG} \\ y_{CG} \\ z_{CG} \end{Bmatrix} \tag{14}$$

$$\begin{Bmatrix} h_{xp} \\ h_{yp} \\ h_{zp} \end{Bmatrix} = I_P \begin{Bmatrix} \dot{p}_P \\ \dot{q}_P \\ \dot{r}_P \end{Bmatrix} + S_P(\boldsymbol{\omega}_{P/I}) I_P \begin{Bmatrix} p_P \\ q_P \\ r_P \end{Bmatrix} \tag{15}$$

$$\begin{Bmatrix} h_{xc} \\ h_{yc} \\ h_{zc} \end{Bmatrix} = I_C \begin{Bmatrix} \dot{p}_C \\ \dot{q}_C \\ \dot{r}_C \end{Bmatrix} + S_C(\boldsymbol{\omega}_{C/I}) I_C \begin{Bmatrix} p_C \\ q_C \\ r_C \end{Bmatrix} \tag{16}$$

Note that the skew symmetric operator $S_B()$ is used in Eqs. (13–16). This operator uses the B frame components of a vector and constructs a matrix such that the multiplication of this matrix by another vector is equivalent to a cross product. The subscript PG denotes the components of vector $\boldsymbol{r}_{\oplus_P \to G}$. Thus, z_{PG} = WL Parafoil. The subscript CG denotes the components of vector $\boldsymbol{r}_{\oplus_C \to G}$. Thus, x_{CG} = SL Tether and z_{CG} = WL Tether. Forces on the canopy include weight, standard aerodynamics, apparent mass aerodynamics, and gimbal joint reaction forces. Forces on the cradle include weight, standard aerodynamics, gimbal joint reaction forces, and the force from the tether. The gimbal joint reaction loads are equal and opposite on the two bodies. Moments on the canopy about its mass center include standard aerodynamics, apparent mass aerodynamics, and gimbal joint constraints. Moments on the cradle about its mass center include gimbal joint constraints and moments from the tether applied offset from the center of mass. The set of four translational and rotational dynamic equations yields 12 scalar equations of motion that can be written in a block form, as shown in the following equations

$$[A]\left\{\begin{matrix} \dot{p}_C \\ \dot{q}_C \\ \dot{r}_C \\ \cdots \\ \dot{p}_P \\ \dot{q}_P \\ \dot{r}_P \\ \cdots \\ \dot{u}_G \\ \dot{v}_G \\ \dot{w}_G \\ \cdots \\ F_{xG} \\ F_{yG} \\ F_{zG} \end{matrix}\right\} = \left\{\begin{matrix} B_1 \\ B_2 \\ B_3 \\ B_4 \end{matrix}\right\} \tag{17}$$

$$A = \begin{bmatrix} m_c S_C(\boldsymbol{r}_{\oplus_C \to G}) & 0 & m_C T_{IC} T_{IP}^T & -T_{IC} \\ 0 & -I_{\mathrm{AM}} S_P(\boldsymbol{r}_{G \to M_P}) + I_H + m_p S_P(\boldsymbol{r}_{\oplus_P \to G}) & m_p + I_{\mathrm{AM}} & T_{IP} \\ I_C & 0 & 0 & -S_C(\boldsymbol{r}_{\oplus_C \to G}) T_{IC} \\ 0 & I_P + S_P(\boldsymbol{r}_{\oplus_P \to M_P})(I_H - I_{\mathrm{AM}} S_P(\boldsymbol{r}_{G \to M_P})) - I_H S_P(\boldsymbol{r}_{G \to M_P}) + I_{AI} & I_H + S_P(\boldsymbol{r}_{\oplus_P \to M_P}) I_{\mathrm{AM}} & S_P(\boldsymbol{r}_{\oplus_P \to G}) T_{IP} \end{bmatrix}$$

in which

$$B_1 = C_C(\boldsymbol{F}_A^C) + C_C(\boldsymbol{F}_W^C) - m_C T_{IC} T_I T_P S_P(\boldsymbol{\omega}_{P/I}) \left\{\begin{matrix} u_G \\ v_G \\ w_G \end{matrix}\right\} + m_C S_C(\boldsymbol{\omega}_{C/I}) S_C(\boldsymbol{\omega}_{C/I}) \left\{\begin{matrix} x_{CG} \\ y_{CG} \\ z_{CG} \end{matrix}\right\} + T_{IC} \left\{\begin{matrix} X_{T_{n_T}} \\ Y_{T_{n_T}} \\ Z_{T_{n_T}} \end{matrix}\right\} \tag{18}$$

$$B_2 = C_P(\boldsymbol{F}_A^P) + C_P(\boldsymbol{F}_W^P) - m_P S_P(\boldsymbol{\omega}_{P/I}) \left\{\begin{matrix} u_G \\ v_G \\ w_G \end{matrix}\right\} - S_P(\boldsymbol{\omega}_{P/I}) \left(I_{\mathrm{AM}} \left\{\begin{matrix} \tilde{u} \\ \tilde{v} \\ \tilde{w} \end{matrix}\right\} + I_H \left\{\begin{matrix} p_P \\ q_P \\ r_P \end{matrix}\right\} \right) + m_P S_P(\boldsymbol{\omega}_{P/I}) S_P(\boldsymbol{\omega}_{P/I}) \left\{\begin{matrix} x_{PG} \\ y_{PG} \\ z_{PG} \end{matrix}\right\} \tag{19}$$

$$B_3 = T_{IC} T_{IP}^T C_P(\boldsymbol{M}_G) - S_C(\boldsymbol{\omega}_{C/I}) I_C \left\{\begin{matrix} p_C \\ q_C \\ r_C \end{matrix}\right\} + S_C(\boldsymbol{r}_{\oplus_C \to F}) T_{IC} \left\{\begin{matrix} X_{T_{n_T}} \\ Y_{T_{n_T}} \\ Z_{T_{n_T}} \end{matrix}\right\} \tag{20}$$

$$B_4 = C_P(\boldsymbol{M}_A^P) + \sum_{i=1}^{N} S_P(\boldsymbol{r}_{\oplus_P \to A_i}) C_P(\boldsymbol{F}_A^i) - C_P(\boldsymbol{M}_G) - [S_P(\boldsymbol{r}_{\oplus_P \to M_P}) S_P(\boldsymbol{\omega}_{P/I}) I_{\mathrm{AM}} + S_P(\boldsymbol{\omega}_{P/I}) I_H] \left\{\begin{matrix} \tilde{u} \\ \tilde{v} \\ \tilde{w} \end{matrix}\right\} - [(S_P(\boldsymbol{r}_{\oplus_P \to M_P}) S_P(\boldsymbol{\omega}_{P/I}) + S_P(\boldsymbol{V}_{M_P/I})) I_H + S_P(\boldsymbol{\omega}_{P/I})(I_P + I_{AI})] \left\{\begin{matrix} p_P \\ q_P \\ r_P \end{matrix}\right\} \tag{21}$$

Matrix A is a block 4×4 matrix in which each element is a 3×3 matrix. Rows 1–3 are forces acting on the cradle mass center expressed in the cradle frame, and rows 7–9 are the moments about the cradle mass center, also in the cradle frame. Rows 4–6 are forces acting on the parafoil mass center expressed in the parafoil frame, and rows 10–12 are the moments about the parafoil mass center, also in the parafoil frame. These equations are inertially coupled due to the selection of the position degrees of freedom as the inertial position vector components of the coupling joint. The constraint force is a quantity of interest to monitor during simulation and therefore is retained in the dynamic equations rather than being algebraically eliminated. The aerodynamic forces on the canopy panels are expressed in terms of lift and drag coefficients, which are functions of the angle of attack α of each panel, $\alpha_i = \tan^{-1}(\tilde{w}_i/\tilde{u}_i)$, as shown in Eqs. (22) and (23). Equation (24) defines the canopy aerodynamic forces in the body reference frame, accounting for the shape of the canopy. Each panel is modeled as a flat plate that is rotated about two angles to approximate the shape of the canopy [6]. For the outboard panels, the lift and drag coefficients are modified by the control deflection δ_i. For all left panels, the control deflection is called the left brake δ_L Similarly, for all right panels, the control deflection is called the right brake δ_R The control system for the left and right brakes is explained in Sec. II.C

$$C_{L,i} = C_{L0,i} + C_{L\alpha,i}\alpha_i + C_{L\delta,i}\delta_i \tag{22}$$

$$C_{D,i} = C_{D0,i} + C_{D\alpha 2,i}\alpha_i^2 + C_{D\delta,i}\delta_i \tag{23}$$

$$C_P(\boldsymbol{F}^P_{A_i}) = \frac{1}{2}\rho S_i T_{P,i}\left(C_{L,i}\sqrt{\tilde{u}_i^2+\tilde{w}_i^2}\begin{Bmatrix}\tilde{w}_i\\0\\-\tilde{u}_i\end{Bmatrix} + C_{D,i}\sqrt{\tilde{u}_i^2+\tilde{v}_i^2+\tilde{w}_i^2}\begin{Bmatrix}\tilde{u}_i\\\tilde{v}_i\\\tilde{w}_i\end{Bmatrix}\right) \tag{24}$$

The aerodynamic force on the cradle from drag is assumed to act at the cradle's center, as shown below using the component operator $C_B(\,)$, which expresses the components of a vector in the B frame

$$C_C(\boldsymbol{F}^C_A) = \frac{1}{2}\rho V_C^2 S_C C_{DC}\begin{Bmatrix}u_{CA}\\v_{CA}\\w_{SA}\end{Bmatrix} \tag{25}$$

Note that u_{CA}, v_{CA}, and w_{CA} are cradle aerodynamic velocities in the cradle frame [8]. It is well known that bodies with small mass-to-volume ratios experience aerodynamic forces and moments from acceleration in fluids [9] and produce apparent mass loads. Because of the relatively small mass-to-volume ratio of parafoils, apparent mass must be considered to properly model dynamic response of these vehicles. For a parafoil with spanwise camber, the apparent mass and inertia can be written as

$$C_P(\boldsymbol{F}^P_{\mathrm{AM}}) = I_{\mathrm{AM}}\begin{Bmatrix}\dot{\tilde{u}}\\\dot{\tilde{v}}\\\dot{\tilde{w}}\end{Bmatrix} + I_H\begin{Bmatrix}\dot{p}_P\\\dot{q}_P\\\dot{r}_P\end{Bmatrix} + S_P(\boldsymbol{\omega}_{P/I})I_{\mathrm{AM}}\begin{Bmatrix}\tilde{u}\\\tilde{v}\\\tilde{w}\end{Bmatrix} + S_P(\boldsymbol{\omega}_{P/I})I_H\begin{Bmatrix}p_P\\q_P\\r_P\end{Bmatrix} \tag{26}$$

$$C_P(\boldsymbol{M}^P_{\mathrm{AM}}) = I_H\begin{Bmatrix}\dot{\tilde{u}}\\\dot{\tilde{v}}\\\dot{\tilde{w}}\end{Bmatrix} + I_{AI}\begin{Bmatrix}\dot{p}_P\\\dot{q}_P\\\dot{r}_P\end{Bmatrix} + S_P(\boldsymbol{\omega}_{P/I})I_H\begin{Bmatrix}\tilde{u}\\\tilde{v}\\\tilde{w}\end{Bmatrix} + (S_P(\boldsymbol{\omega}_{P/I})I_{AI} + S_P(\boldsymbol{V}_{M_{P/I}})I_H)\begin{Bmatrix}p_P\\q_P\\r_P\end{Bmatrix} \tag{27}$$

which uses the aerodynamic velocity of the apparent mass as given by the following equation:

$$\begin{Bmatrix}\tilde{u}\\\tilde{v}\\\tilde{w}\end{Bmatrix} = \begin{Bmatrix}u_G\\v_G\\w_G\end{Bmatrix} + S_P(\boldsymbol{\omega}_{P/I})\begin{Bmatrix}x_{GM_p}\\y_{GM_p}\\z_{GM_p}\end{Bmatrix} \tag{28}$$

The subscript GM_P denotes the components of vector $\boldsymbol{r}_{\oplus_P \to M_p}$. The inertia matrix I_{AM} is the basic apparent mass matrix, I_{AI} is the basic apparent inertia matrix, and I_H is the spanwise camber matrix

$$I_{\mathrm{AM}} = \begin{bmatrix}A&0&0\\0&B&0\\0&0&C\end{bmatrix} \tag{29}$$

$$I_{AI} = \begin{bmatrix}P&0&0\\0&Q&0\\0&0&R\end{bmatrix} \tag{30}$$

$$I_H = \begin{bmatrix}0&H&0\\H&0&0\\0&0&0\end{bmatrix} \tag{31}$$

The applied moment on the parafoil and cradle contains contributions from the coupling joint's resistance to twisting. The resistance to twisting of the coupling joint is modeled as a rotational spring and damper

$$C_P(\boldsymbol{M}_G) = \begin{Bmatrix}0\\0\\K_G(\psi_P-\psi_C)+C_G(\dot{\psi}_P-\dot{\psi}_C)\end{Bmatrix} \tag{32}$$

Finally, the weight force vectors on both the parafoil and cradle in their respective body axes are given in the following equations

$$C_P(\boldsymbol{F}^P_W) = m_P g\begin{Bmatrix}-s_{\theta_p}\\s_{\phi_p}c_{\theta_p}\\c_{\phi_p}c_{\theta_p}\end{Bmatrix} \tag{33}$$

$$C_C(\boldsymbol{F}^C_W) = m_C g\begin{Bmatrix}-s_{\theta_C}\\s_{\phi_C}c_{\theta_C}\\c_{\phi_C}c_{\theta_C}\end{Bmatrix} \tag{34}$$

B. Tether Model

Figure 3 depicts the tether with both ends attached to the tow vehicle at point R and the cradle at point F. The tether is approximated as n_T beads and n_T+1 elastic elements. A standard linear solid viscoelastic element is used to connect beads, as depicted in the enlarged portion of Fig. 3 [10–13]. Collectively, the motion of the beads defines the motion of the tether line. Each bead on the tether is a point mass possessing three translational degrees of freedom. Forces that drive the motion of the beads include bead weight, aerodynamic forces, and adjacent viscoelastic element line forces.

The dynamic equations for one bead on the tether are structurally the same for all beads, and so the formulas to follow are shown only for the ith bead on the tether line

$$\begin{Bmatrix}\ddot{x}_{T_i}\\\ddot{y}_{T_i}\\\ddot{z}_{T_i}\end{Bmatrix} = \frac{1}{m_i}\begin{Bmatrix}X_{T_i}-X_{T_{i+1}}+X_{Di}\\Y_{T_i}-Y_{T_{i+1}}+Y_{Di}\\Z_{T_i}-Z_{T_{i+1}}+Z_{Di}\end{Bmatrix} + \begin{Bmatrix}0\\0\\g\end{Bmatrix} \tag{35}$$

In Eq. (35), m_i is the mass of the ith bead on a tether element, and g is the gravitational constant. The terms X_{T_i}, Y_{T_i}, Z_{T_i} and $X_{T_{i+1}}$, $Y_{T_{i+1}}$, $Z_{T_{i+1}}$ represent the viscoelastic line force vector components expressed in the inertial reference frame of the tether elements adjacent to the ith bead. The line forces are caused by strain of the tether and are directed parallel to the line. Tether line flexibility generates resistive stiffness and damping forces caused by tether line extension and extension rate. The terms X_{Di}, Y_{Di}, and Z_{Di} are aerodynamic drag forces applied to each bead. To compute the viscoelastic line forces, it is useful to define a tether element position and velocity difference vector for each tether element. The difference vectors are formed by subtracting the position or velocity components of the $i+1$ tether bead (or ending connection) from

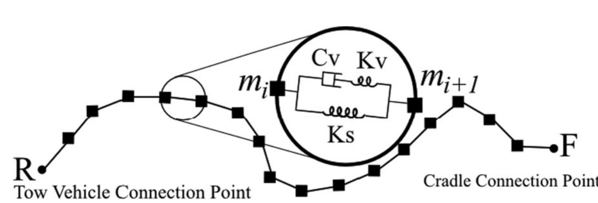

Fig. 3 Tether schematic.

the ith tether bead component (or beginning connection). This results in $n_T + 1$ difference vectors for the tether line. The terms Δx_{T_i}, Δy_{T_i}, and Δz_{T_i} represent the components of the position difference vectors, whereas the velocity difference vectors are used to construct the stretch rate $\dot{s}_{T_i}$. Using the tether element position difference and velocity difference data, an expression for the elastic line force can be directly formed

$$\begin{Bmatrix} X_{T_i} \\ Y_{T_i} \\ Z_{T_i} \end{Bmatrix} = \frac{F_{T_i}}{s_{T_i}} \begin{Bmatrix} \Delta x_{T_i} \\ \Delta y_{T_i} \\ \Delta z_{T_i} \end{Bmatrix} \tag{36}$$

Equations (37) and (38) provide expressions for the elastic line force F_{T_i} in terms of the strain and strain rate of the viscoelastic tether element

$$\dot{F}_{T_i} + \frac{K_v}{C_v} F_{T_i} = \begin{cases} (K_s + K_v)\dot{s}_{T_i} + \frac{K_v K_s}{C_v}(s_{T_i} - L_T), & \text{if } s_{T_i} - L_T > 0 \\ 0, & \text{if } s_{T_i} - L_T \le 0 \end{cases} \tag{37}$$

$$s_{T_i} = \sqrt{\Delta x_{T_i}^2 + \Delta y_{T_i}^2 + \Delta z_{T_i}^2} \tag{38}$$

In Eq. (37), K_v, C_v, and K_s are the viscous stiffness, viscous damping, and static stiffness coefficients respectively, for a viscoelastic line element. Also, L_T is the nominal unstretched line length of a tether element. All individual tether elements have the same static and viscous stiffness coefficients, viscous damping coefficient, and unstretched line length. The first condition in Eq. (37) represents the normal tension condition between two adjacent beads. In this case, the distance between the two adjacent beads is greater than the unstretched elastic tether element length, and a nonzero tension force in the tether element persists. The second condition in Eq. (37) is the slack condition. It stipulates that, when the unstretched elastic tether element length is greater than the distance between two adjacent beads, the elastic force declines at a rate dictated by the term $(K_v/C_v)F_{T_i}$.

Edge point position and velocity of the tether is required for viscoelastic line force computation. For edge points of the tether that are fixed on a body of the system, expressions for the position and velocity are formed from the motion of the connection point on the body. Thus, the first element position and velocity is equal to the position and velocity of the point R governed by the towed body motion. The $n_T + 1$ element position and velocity is given by the position and velocity of the cradle at point F. Mathematically, this can be written using the following equations:

$$\begin{Bmatrix} x_{T_1} \\ y_{T_1} \\ z_{T_1} \end{Bmatrix} = \begin{Bmatrix} x_R \\ y_R \\ z_R \end{Bmatrix}, \qquad \begin{Bmatrix} x_{T_{n_T+1}} \\ y_{T_{n_T+1}} \\ z_{T_{n_T+1}} \end{Bmatrix} = \begin{Bmatrix} x_F \\ y_F \\ z_F \end{Bmatrix} \tag{39}$$

$$\begin{Bmatrix} \dot{x}_{T_1} \\ \dot{y}_{T_1} \\ \dot{z}_{T_1} \end{Bmatrix} = \begin{Bmatrix} \dot{x}_R \\ \dot{y}_R \\ \dot{z}_R \end{Bmatrix}, \qquad \begin{Bmatrix} \dot{x}_{T_{n_T+1}} \\ \dot{y}_{T_{n_T+1}} \\ \dot{z}_{T_{n_T+1}} \end{Bmatrix} = \begin{Bmatrix} \dot{x}_F \\ \dot{y}_F \\ \dot{z}_F \end{Bmatrix} \tag{40}$$

The aerodynamic force on the tether line includes skin-friction drag along the tether line and flat-plate drag perpendicular to the tether line [14]. To determine the tether drag, it is useful to define a unit vector with measure numbers given by

$$\begin{Bmatrix} r_{x_i} \\ r_{y_i} \\ r_{z_i} \end{Bmatrix} = \frac{1}{L_T} \begin{Bmatrix} \Delta x_{T_i} \\ \Delta y_{T_i} \\ \Delta z_{T_i} \end{Bmatrix} \tag{41}$$

The skin-friction and flat-plate drag for each element are given by

$$D_{S_i} = \frac{1}{2}\rho V_{S_i} |V_{S_i}| A_w C_S \tag{42}$$

$$D_{F_i} = \frac{1}{2}\rho V_{F_i}^2 A_w C_F \tag{43}$$

in which C_S and C_F are the skin-friction and flat-plate drag coefficients, V_{S_i} and V_{F_i} are the magnitude of velocity of the ith bead parallel and normal to the ith tether element, and A_w is the wetted area of the ith bead. The tether bead aerodynamic forces expressed in the inertial frame are then

$$\begin{Bmatrix} X_{D_i} \\ Y_{D_i} \\ Z_{D_i} \end{Bmatrix} = D_{S_{i+1}} \begin{Bmatrix} r_{x_{i+1}} \\ r_{y_{i+1}} \\ r_{z_{i+1}} \end{Bmatrix} + D_{S_i} \begin{Bmatrix} r_{x_i} \\ r_{y_i} \\ r_{z_i} \end{Bmatrix} + \frac{D_{F_{i+1}}}{V_{F_{i+1}}} \begin{Bmatrix} V_{F,x,i+1} \\ V_{F,y,i+1} \\ V_{F,z,i+1} \end{Bmatrix} + \frac{D_{F_i}}{V_{F_i}} \begin{Bmatrix} V_{F,x} \\ V_{F,y} \\ V_{F,z} \end{Bmatrix} \tag{44}$$

C. Control System

For system configurations using active control, a proportional plus derivative control law is employed using canopy roll-angle feedback. Canopy roll-angle feedback is obtained by measuring the roll angle of the risers in combination with the roll angle of the cradle. The roll angle of the risers can be seen in Fig. 4, in which both the left (ϕ_L) and right (ϕ_R) riser angles are measured from the vertical cradle axis. During initial experimental tests, it was found that potentiometers could be placed on either side of the cradle to obtain left and right riser angles with error levels under 10 deg. During a separate design iteration, the yaw angle was used as feedback; however, no benefit was found when using the yaw angle as feedback. Therefore, the control system presented here was found to be the easiest to implement on a practical system.

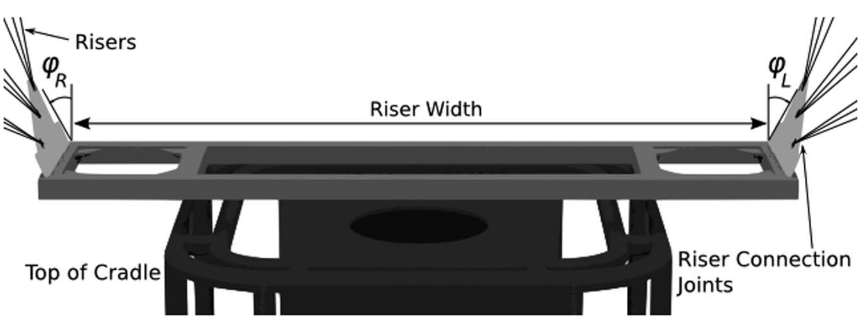

Fig. 4 Example cradle enlarged to show riser roll angles and riser width.

Using the riser roll angles, the canopy roll angle is then found using

$$\phi_{P_i} = 0.5(\phi_L + \phi_R) + \phi_C \tag{45}$$

in which ϕ_C is the cradle roll angle. The canopy roll angle is processed by a derivative filter using the equation below to obtain the derivative of the canopy roll angle

$$\dot{\phi}_{P_i} = \frac{2(\phi_{P_i} - \phi_{P_{i-1}}) + \dot{\phi}_{P_{i-1}}(2\tau - \Delta t)}{2\tau + \Delta t} \tag{46}$$

in which τ is the inverse of the derivative filter cutoff frequency and Δt is the time step between calculations. Using these two values, a PD controller can be developed to create left and right brake deflection commands

$$\Delta = K_P \phi_{P_i} + K_D \dot{\phi}_{P_i} \tag{47}$$

$$\delta_{L,\mathrm{COMM}} = |\Delta| + \delta_S, \qquad \delta_{R,\mathrm{COMM}} = \delta_S, \qquad \Delta \geq 0 \tag{48}$$

$$\delta_{R,\mathrm{COMM}} = |\Delta| + \delta_S, \qquad \delta_{L,\mathrm{COMM}} = \delta_S, \qquad \Delta < 0 \tag{49}$$

The control scheme presented here seeks to null the roll angle of the canopy. If the signal Δ is positive, the left brake is applied and the right brake returns to the nominal symmetric brake value. If Δ is negative, the opposite occurs. The net result is that the canopy resists any nonzero roll angle that can reduce the onset of lockout. Note that each brake is modeled as a first-order system using the equations below

$$\dot{\delta}_R = T(\delta_{R,\mathrm{COMM}} - \delta_R) \tag{50}$$

$$\dot{\delta}_L = T(\delta_{L,\mathrm{COMM}} - \delta_L) \tag{51}$$

in which T is the time constant. The left and right brakes are included in the model using Eqs. (22) and (23), in which $\delta_i = \delta_R$ for all right panels and $\delta_i = \delta_L$ for all left panels. A rate limiter was also added to avoid nonrealistic motion such that $|\dot{\delta}_i| \leq \omega_{\max}$.

III. Simulation Setup

The example parafoil canopy used in this analysis is based on the Spiruline L made by Little Cloud, which has a wingspan of 8.8 m, a chord of 2.1 m, and an area of 18.5 m^2. The canopy weight is 3.7 kg, with moments of inertia of 45.53, 9.65, and 45.86 $\mathrm{kg \cdot m^2}$ along the x, y, and z axes, respectively. The apparent mass coefficients A, B, and C are 0.984, 0.0988, and 36.405 kg, respectively. The rotational apparent mass coefficients P, Q, and R are 194.21, 7.53, and 6.91 $\mathrm{kg \cdot m}$ respectively. The distance from the gimbal joint to the canopy center of mass is WL Parafoil $= -5.75$ m.

The canopy is split into nine panels to approximate the curvature of the wing. The canopy zero lift aerodynamic coefficients for each panel are set to that of a NACA 0015, thus $C_{L0} = 0.0$ and $C_{D0} = 0.018$. The lift and drag profiles for each panel are set such that the canopy has a nominal glide ratio of 8 when the incidence angle of the canopy is set to 3.5 deg. This gives a nominal angle of attack on the canopy of 8 deg when gliding without brake deflection with a cradle weight of 80 kg, as given by the Little Cloud specifications. Using these parameters, $C_{L\alpha} = 5.203$ and $C_{D\alpha 2} = 1.689$. The nominal symmetric brake deflection is set to 40% of its maximum deflection. The maximum brake deflection is 68 cm, thus 40% is 25.2 cm. To obtain the brake coefficients, an experiment was performed in which the tension value in the line was measured using a load sensor. This tension value was matched in simulation by varying $C_{L\delta}$. The control coefficient for lift was set to $C_{L\delta} = 0.7$. During canopy brake deflection, the L/D ratio is kept reasonably constant, thus $C_{D\delta} = 0.064$. Brake deflections are governed by a first-order filter with a time constant of 2.0, which was also obtained by a simple experiment in which the brakes were initially set to zero and commanded to 100%. The brakes are rate limited to 16 cm/s. The control system gains are set such that $K_P = 4$, $K_D = 1$, $\tau = 0.1$ s, and $f = 10$ Hz.

The canopy is carrying a custom-made cradle with an area of 0.4337 m^2 and a weight of 90 kg. The moments of inertia are 9.38, 6.05, and 6.24 $\mathrm{kg \cdot m^2}$ along the x, y, and z axes, respectively. The distance from the gimbal joint to the cradle center of mass is WL Cradle $= 0.47$ m. The cradle flat-plate drag is equal to 1.0. The tether connection point is set to SL Tether $= 0.3$ m and WL Tether $= 0.23$ m. The yaw stiffness and damping of the connection coupling joint is set to 30 $\mathrm{N/(m \cdot rad)}$ and 10 $\mathrm{N \cdot m/(rad/s)}$.

The tether line is based on a liquid crystal polymer fiber made by Vectran with mass per unit length of 0.00272 kg/m. The total unstretched length of the tether is 478 m, which results in a total weight of 1.3 kg. The diameter of the tether is 0.00196 m and has a maximum stiffness load of 4,884 N at 3.8% elongation. The flat-plate and skin-friction drag coefficients are set to 1.0. The number of beads used to discretize the tether was set to 10 beads, based on a convergence analysis run during initial simulations.

IV. Example Simulation Results

Consider a scenario in which the canopy is trimmed to a steady, level condition behind the tow vehicle, which has a velocity of 12.86 m/s. In this scenario, the pitch angle of the canopy is 5.09 deg, the pitch angle of the cradle is -5.45 deg and the angle of the tether with respect to the vertical axis is 16.12 deg. To induce the lockout condition, the parafoil experiences a constant 2 m/s side wind, and the yaw stiffness is reduced to 20 $\mathrm{N \cdot m/rad}$. This reduction in yaw stiffness is a direct cause of lockout and is explained in Sec. V.A. Figures 5–7 show the canopy roll, pitch, and yaw angles with and without the control system enabled. These figures also show an enlarged figure from 0 to 20 s to show detail. The initial response of the entire system is to roll away from the disturbance and turn into the wind. This offset in roll angle causes the system to sideslip, which initially causes the roll angle to return to 0 deg; however, the lateral deflection increases tension on the line, which causes the roll angle to increase again until it rolls past 30 deg. Meanwhile, due to the increase in the canopy roll angle, the canopy yaw angle begins to increase around 80 s until it reaches a value greater than 30 deg. Without active control, these angles grow without bound. Thus, the system is unstable without control. However, with the control system activated, the roll angle is quickly returned to and maintained at 0 deg.

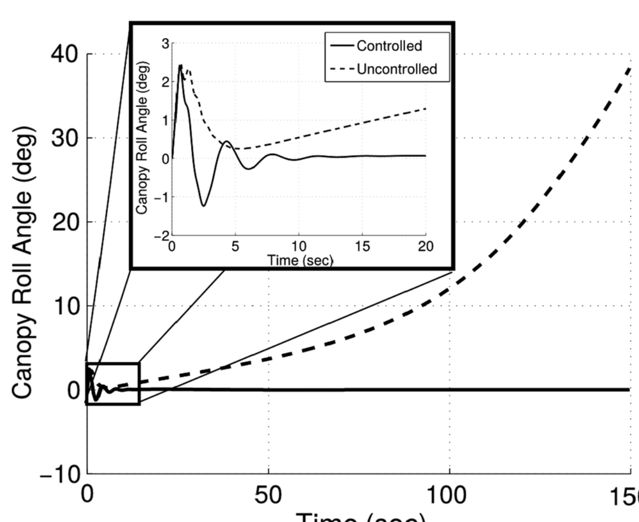

Fig. 5 Canopy roll angle (deg) vs time (s) with enlarged insert to show detail.

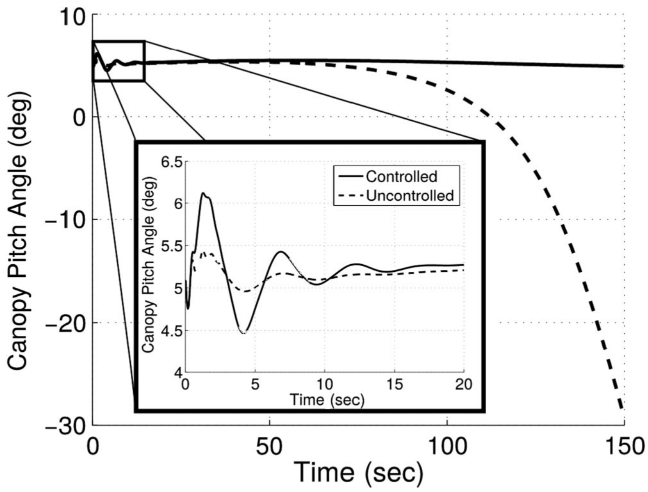

Fig. 6 Canopy pitch angle (deg) vs time (s) with enlarged insert to show detail.

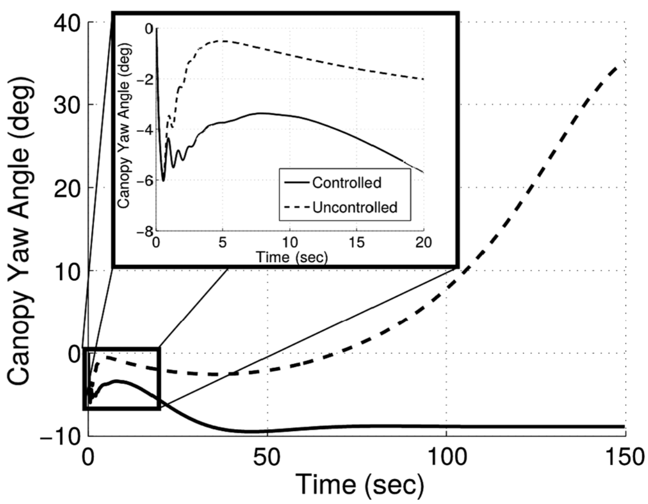

Fig. 7 Canopy yaw angle (deg) vs time (s) with enlarged insert to show detail.

This allows the yaw angle to attain an equilibrium value of about −9 deg, which corresponds to the canopy turning into the wind.

Figure 8 shows brake deflection during this event, as well as an enlarged figure. The nominal brake deflection is 40%; and, with the control system activated, roughly 15% extra control effort is needed to stabilize the system. Note that the brakes do not immediately return to nominal when commanded to zero due to the first-order nature of the brake lines. The net result is that left and right brakes can be deflected simultaneously. The lockout condition explained here can also be visualized easily in three dimensions if the parafoil is plotted with respect to the tow point as shown in Fig. 1.

V. Stability Analysis for Towed Systems

Simulation results shown previously (Figs. 5–8) for the passive configuration provide an example of an unstable lockout condition in which the canopy turns away from the tether line of action and fails to remain airborne. The overall geometry of the parafoil and cradle system alters the onset of lockout. This includes the connection joint properties, connection point of the tether on the cradle, the distance between the connection coupling joint to the cradle and canopy, and, finally, cradle weight. Stability of the system as a function of these parameters is determined through analysis of numerically linearized models about an equilibrium point. To obtain the numerically linearized models, the trim state of a particular configuration is obtained by integrating the equations of motion until the system reaches steady state with all state derivatives (except the forward

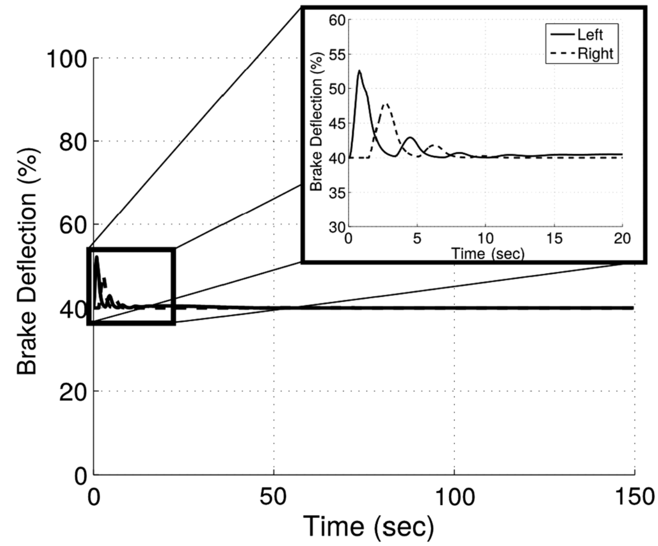

Fig. 8 Brake deflection (%) vs time (s) with enlarged insert to show detail.

velocity) less than 1×10^{-8}. This trimming procedure was found to work robustly for all configurations examined. Once the trim state of a configuration is obtained, a linear time-invariant (LTI) model is obtained numerically using central finite differencing to compute the Jacobian of the nonlinear model [15]. Each state is perturbed from trim by 1×10^{-6} to compute numerical derivatives to produce an 18-state LTI model. This results in 18 associated eigenvalues (modes) and eigenvectors (mode shapes). If the real part of any of these 18 eigenvalues is positive, the system is unstable. In this analysis, a lateral real mode becomes unstable under certain circumstances. The dominant state variables of this mode are lateral quantities, including lateral translational motion, parafoil roll angle, parafoil yaw angle, cradle yaw angle, and cradle roll angle. Subsequent analyses refer to this mode as the lockout mode.

A. Connection Coupling Joint

The connection joint has a built in stiffness and damping along the yaw axis of the cradle and canopy. The riser width, or the distance between the left and right risers (Fig. 4), is the main driver for the stiffness of this joint. Increasing the width of the risers increases the yaw stiffness. Figure 9 shows the lockout mode as a function of yaw stiffness and damping for both the uncontrolled and controlled configurations.

Notice that the yaw damping coefficient has little effect on this mode. However, this lateral mode becomes positive when the

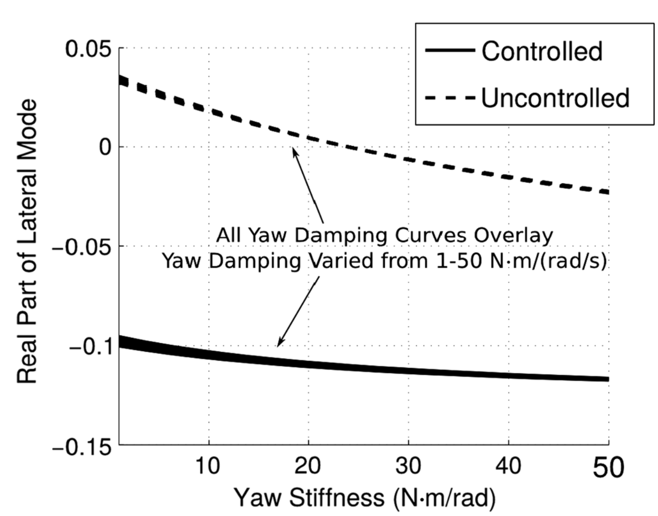

Fig. 9 Lockout mode vs yaw stiffness.

stiffness of the joint is reduced beyond about 25 N · m/rad. The results here make intuitive sense due to the nature of the tether force. The tether pulls on the cradle and causes the cradle to turn toward the tether line of action. This difference between the cradle and canopy heading angle induces a yaw moment on the canopy, which serves to orient the canopy toward the tether line of action. If the yaw moment is not large enough, the canopy will grow without bound rather than reach steady state, and lockout will occur. Figure 9 also shows the result of enabling the control system while changing the yaw stiffness and damping. This figure indicates that the lateral mode is always negative and therefore stable with the control system enabled. With the control system disabled, the stiffness must be larger than 25 N · m/rad. The explanation of this result is due to the roll stability of the canopy. The canopy itself has a tendency to turn itself into the wind; however, the roll dynamics are faster than the yaw dynamics. This can be seen in Fig. 5. The yaw mode of the canopy is inherently stable unless the roll angle of the canopy is greater than a critical value. That is, the yaw angle is a function of the roll angle. When the roll angle is well behaved and bounded, the yaw angle settles to a finite value. Once the roll angle reaches a critical angle, the yaw angle no longer settles and begins to grow without bound. Thus, active control of the roll angle maintains the canopy to remain below critical levels, and thus the system will have ample time to turn itself into the wind. With the control system disabled, the only restoring force is done by the yaw stiffness of the coupling joint, which must be increased to orient the system into the wind.

B. Tether Connection Point

A main driver of lockout mode stability is the canopy's tendency to yaw toward the tether line. This is accomplished by the tether line force yawing the cradle, creating an offset in yaw angle between the cradle and the canopy. This difference in yaw angle induces a moment in the canopy, which in turn yaws toward the tether. This restoring moment placed on the cradle can be altered by increasing the stiffness of the connection coupling joint but also by changing the location of the tether attachment point. The tether attachment point can be seen in Fig. 2 and is denoted as point F. Figure 10 shows the stability boundaries as a function of the tether attachment point, as well as small figures to indicate the change in tether attachment point. This is equivalent to moving point F in Fig. 2. The dashed line in Fig. 10 represents the stability boundary for the uncontrolled system, and the solid line represents the stability boundary for the controlled system. The coordinates in Fig. 10 are the distances from the center of mass of the cradle (0, 0) to the tether attachment point. Here, it is clear that a forward attachment point is critical for a passively stable system. The boundary is angled because the tether line of action is angled at 16 deg from the vertical. The explanation for this forward connection point can be explained by examining the yaw moment placed on the cradle. If the tether is attached far forward, a sideslip angle will force the cradle to turn toward the tether line of action. Provided there is enough yaw stiffness, the offset in yaw angle between the canopy and the cradle will cause the canopy to turn toward the tether line of action as well. If the tether is connected closer to the center of mass or even behind it, this yawing tendency will be removed and the system becomes unstable. The control system here acts to prevent this instability; however, there is a point at which the control system is not capable of achieving stability. Viewing Fig. 11, the magnitude of the lateral eigenvalue can be seen for both the controlled system (left) and the uncontrolled system (right). When the tether is attached in the upper left corner, the eigenvalue becomes positive and quite large compared with the stable region. Physically, the upper left corner represents an area where the cradle flips upside down, representing a nonpractical connection point. The solid and dashed lines in the figure represent the stability boundaries between a positive and negative eigenvalue.

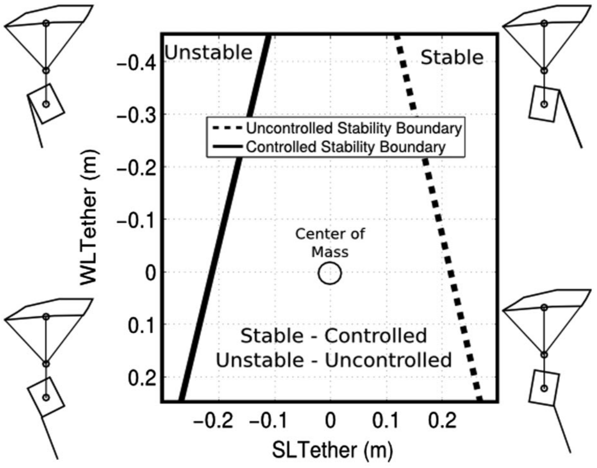

Fig. 10 Lockout mode stability boundaries as a function of tether attachment point.

C. Canopy and Cradle Rigging Length

Another important attribute for lockout mode stability is the canopy's tendency to remain upright during maneuvers. A way to alter these dynamics is to change the rigging length between the gimbal joint and the cradle center of mass (WL Cradle) and the rigging length from the gimbal joint to the parafoil center of mass (WL Parafoil) as shown in Fig. 2. Changing these parameters will change the roll inertia of the system, which directly affects the roll response of the system. Figure 12 shows the dynamic stability boundaries versus canopy and cradle rigging lengths, as well as small graphics indicating the overall change in geometry. The figure on the left shows lockout mode stability boundaries for the control system disabled and enabled. The graph clearly indicates that the upper right corner is the most stable region. This region corresponds to the system having the most roll inertia by increasing the canopy and cradle rigging lengths. Moving from the top right corner to the lower left corner shrinks the entire system and causes the system to become more and more unstable. However, with the control system enabled,

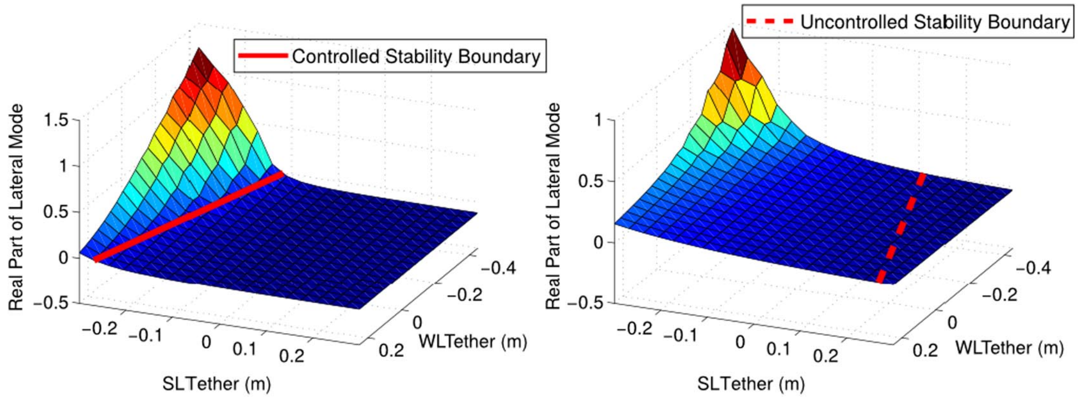

Fig. 11 Lockout mode as a function of tether attachment point: (left) controlled; (right) uncontrolled.

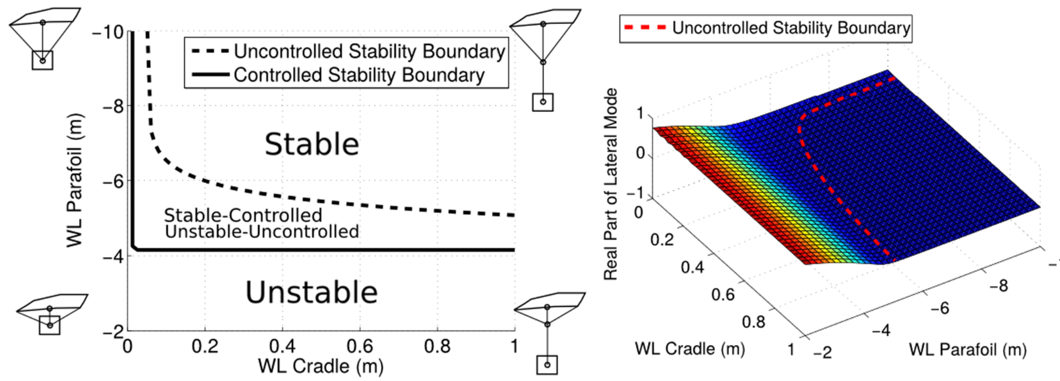

Fig. 12 (Left) Lockout mode stability Boundaries and (right) uncontrolled lateral mode as a function of canopy and cradle rigging length (m).

this stability boundary shifts toward the lower left corner to increase the size of the stable region.

The right figure shows the value of the real part of the lateral eigenvalue and the stability boundary for the uncontrolled system. This graph indicates that the canopy and cradle rigging length play a large role in the overall stability of the system.

D. Cradle Mass and Symmetric Brakes

In addition to the geometry of the system, the tension in the tether plays an important role in the determination of stability. A simple way to change the tension in the tether is to deflect the symmetric brakes away from their nominal position of 40%. Increasing symmetric brakes on a parafoil increases tension due to an increase in lift on the canopy. In addition, the tension can be altered through the cradle mass. The cradle mass affects the tension in the tether inversely. A decrease in the cradle mass increases the tension in the tether. Initially, the lift in the canopy is equal to the weight of the entire system plus the tension. When the mass of the canopy is reduced, the lift stays constant. Thus, the tension must increase to balance out the forces applied to the system. Figure 13 shows the lockout mode stability boundary (left) versus cradle mass and symmetric brake deflection. The upper right region corresponds to a region where there is not enough lift produced on the canopy, and the system cannot achieve trim. The left region corresponds to a zone of high tension that leads to lockout mode instability. This figure also shows the lockout mode for the uncontrolled system (right). Here, it is clear that the eigenvalue becomes positive for high line tension that directly correlates to the lockout condition seen in the literature [6].

However, with the control system enabled, the system is stable for all configurations except the upper right region. Figure 14 shows the equilibrium tension value as a function of both the mass of the cradle and the symmetric brake deflection. The nominal configuration of 90 kg and 40% symmetric brake has a tension of about 680 N. Increasing symmetric brake deflection or decreasing the cradle mass increases the tension in the tether. However, the lift produced by the

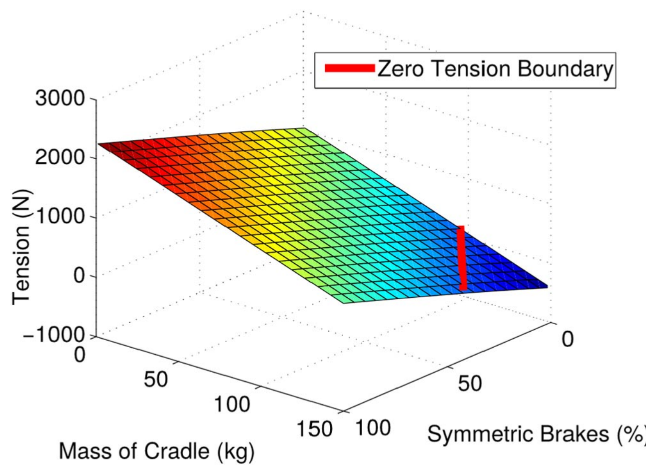

Fig. 14 Tension (N) vs cradle mass (kg) and symmetric brake deflection (%).

canopy is largely a function of the symmetric brake deflection. Thus, when the symmetric brake deflection is at 0%, the lift produced on the canopy is at its lowest. This reduction in lift causes a decline in roll stability, which produces the slight taper in the stability contour in Fig. 13.

VI. Conclusions

A dynamic analysis of the lockout condition exhibited by towed parafoil systems has been investigated here, with an emphasis placed on geometric changes that can be made to the system to reduce the onset of lockout as well as a control system that further reduces the onset of lockout. Simulation results revealed that a minimum yaw stiffness is required in the gimbal joint. In addition, moving the tether

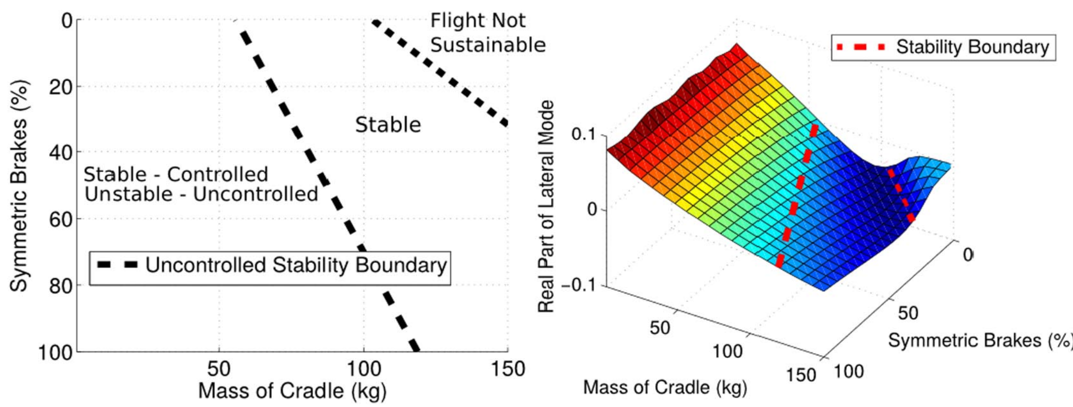

Fig. 13 (Left) Lockout mode stability boundaries and (right) uncontrolled lateral mode as a function of cradle mass (kg) and symmetric brake deflection (%).

connection point forward of the center of mass of the cradle seeks to orient the cradle toward the tether. This tendency, coupled with the high stiffness in the gimbal joint, orients the parafoil into the wind, which inhibits lockout from occurring. Furthermore, the roll inertia of the parafoil also directly affects the lockout condition due to the coupled nature between the yaw and roll modes of the canopy. Here, a large distance between the parafoil and cradle results in a larger roll inertia, which inhibits lockout from occurring. Finally, the tension in the tether was also found to be a driver of lockout. Increasing the tension in the tether, by either reducing the mass of the cradle or increasing symmetric brake deflection, results in a less stable system. All of these boundaries were shown to increase by installing a left and right brake deflection controller using feedback from the canopy roll angle. Active control of the roll mode of the canopy expanded the stability envelope for all configurations investigated. Note, however that no claim was made about the tracking error performance of this system. If errors are introduced into the system, the tracking error of the system will increase. Further simulations revealed that a bias in the roll angle could negate the effects of the active control system. If the bias in the roll angle is larger than 15 deg, the control system is incapable of keeping the system airborne. However, if the error in the feedback signals is below this critical value, the stability envelope is preserved at the cost of poor tracking performance. These results were revealed using a sophisticated 9 DOF parafoil and cradle model coupled to a viscoelastic tether model. A linearization procedure was also conducted in order to compute the lockout mode as a function of geometric changes while keeping the tether parameters fixed. An interesting study, therefore, would be to investigate tether parameters such as tether diameter, stiffness, or length and to examine their effects on the lockout instability. Still, the addition of the 9 DOF model highlighted unstable modes caused by the cradle and parafoil obtaining different orientations during flight. In Puranik et al. [4], the results indicate that, if the windspeed experienced by the system is too large, the system will be unable to place the vehicle in trim. The work presented here provides a nice complement by analyzing the fundamental modes based on geometric changes to the system. Plant stability, coupled with the stability boundaries in [4], should create a nice picture of what geometric parameters can be varied to stabilize the system and what winds can be experienced before lockout occurs.

References

[1] Williams, P., Lansdorp, B., Ruiterkamp, R., and Ockels, W., "Modeling, Simulation, and Testing of Surf Kites for Power Generation" *AIAA Modeling and Simulation Technologies Conference and Exhibit*, AIAA Paper 2008-6693, Aug. 2008.
doi:10.2514/6.2008-6693

[2] Costello, M., and Slegers, N., "On the Use of Rigging Angle and Canopy Tilt for Control of a Parafoil and Payload System," *AIAA Atmospheric Flight Mechanics Conference and Exhibit*, AIAA Paper 2003-5609, Aug. 2003.
doi:10.2514/6.2003-5609

[3] Puranik, A., Parker, G., Passerello, C., Bird, J., Yakimenko, O., and Kaminer, I., "Modeling and Simulation of a Ship Launched Glider Cargo Delivery System," *AIAA Guidance, Navigation, and Control Conference and Exhibit*, AIAA Paper 2006-6791, Aug. 2006.
doi:10.2514/6.2006-6791

[4] Puranik, A., "Dynamic Modeling, Simulation and Control Design of a Parafoil-Payload System for Ship-Launched Aerial Delivery System (SLADS)," Ph.D. Dissertation, Michigan Technological Univ., Houghton, MI, 2011.

[5] Terink, E., Breukel, J., Schmehl, R., and Ockels, W., "Flight Dynamics and Stability of a Tethered Inflatable Kiteplane," *Journal of Aircraft*, Vol. 39, No. 1, 2011, pp. 503–513.
doi:10.2514/1.C031108

[6] Slegers, N, and Costello, M, "Aspects of Control for a Parafoil and Payload System," *Journal of Guidance, Control, and Dynamics*, Vol. 26, No. 6, 2003, pp. 898–905.
doi:10.2514/2.6933

[7] Bernard, E., "Dynamics of Atmospheric Flight," Dover Publ., Mineola, NY, 2005, pp. 104–150.

[8] Ward, M., Montalvo, C., and Costello, M., "Performance Characteristics of an Autonomous Airdrop System in Realistic Wind Environments" *AIAA Atmospheric Flight Mechanics Conference*, AIAA Paper 2010-7510, Aug. 2010.
doi:10.2514/6.2010-7510

[9] Lissaman, P., and Brown, G., "Apparent Mass Effects on Parafoil Dynamics," *AIAA Aerospace Design Conference*, AIAA Paper 1993-1236, 1993.
doi:10.2514/6.1993-1236

[10] Kyle, J., and Costello, M., "Comparison of Measured and Simulated Motion of a Scale Dragline Excavation System," *Mathematical and Computer Modeling*, Vol. 44, Nos. 9–10, Nov. 2006, pp. 816–833.
doi:10.1016/j.mcm.2006.02.015

[11] Kim, E., and Vadali, S., "Modeling Issues Related to Retrieval of Flexible Tethered Satellite Systems," *Journal of Guidance, Control, and Dynamics*, Vol. 18, No. 5, 1995, pp. 1169–1176.
doi:10.2514/3.21521

[12] Jones, S.P., and Krausman, J. A., "Nonlinear Dynamic Simulation of a Tethered Aerostat," *Journal of Aircraft*, Vol. 19, No. 8, 1982, pp. 679–686.
doi:10.2514/3.57449

[13] Quisenberry, J., and Arena, A., "Discrete Cable Modeling and Dynamic Analysis," *44th AIAA Aerospace Sciences Meeting and Exhibit*, AIAA Paper 2006-424, Jan. 2006.
doi:10.2514/6.2006-424

[14] Frost, G., and Costello, M., "Improved Deployment Characteristics of a Tether-Connected Munition System," *Journal of Guidance, Control, and Dynamics*, Vol. 24, No. 3, 2001, pp. 547–554.
doi:10.2514/2.4745

[15] Phillips, W., "Mechanics of Flight," 2nd ed., Wiley, Hoboken, NJ, 2010, pp. 715–952.